Impact of Dual Matrix Porosity in Sandstone on Fluid Distribution and Flow Properties

Yingxue Wang* and *Serge V.* Galley

Shell USA, Inc.

Abstract. In a deep-water sandstone reservoir in the Gulf of Mexico, minerology and petrographic study show an alternating, sorted bimodal grain size distribution and continuous clay coating. Saturation functions (i.e. capillary pressure and relative permeability) assuming single porosity system would introduce large errors in modelling fluid distribution and flow properties. A dual matrix porosity approach is presented to characterize core samples using a range of data from nuclear magnetic resonance (NMR) to core measurements and petrography. The total porosity consists of contributions from macro- and meso- porosities, respectively. A dual porosity capillary pressure model is developed using modified Brooks-Corey function to properly describes the initial oil saturation distribution in both porosity systems. The capillary pressure model is then extended to model the imbibition process to assess the wettability condition. Numerical simulations are used to evaluate the impact of the saturation function on the oil-water displacement. This study demonstrated that heterogeneity greatly affects the fluid distribution and the wettability in the core scale. Contribution of the meso-porosity to the total flow varies and should be properly accounted for in reservoir simulations to model water development and production.

1 Introduction

Historically, most sandstone reservoirs are characterized as a single-porosity system; they are relatively homogenous with inter-granular pores. Conventionally, the initial fluid distribution and the flow properties in sandstone reservoirs are modelled by saturation functions describing a single-porosity system. For example, a Thomeer [1] or Brooks-Corey [2] function is often used to model the primary drainage capillary pressure or the initial saturation distribution. And Corey relative permeability functions are used to model the fluid displacement. In dynamic simulations, for a sandstone reservoir under strong aquifer drive or water flood, impacts of the imbibition capillary pressure are often ignored. Those saturation functions are normally calibrated to special core analysis (SCAL) results. Under the same concept, in the interpretation of a SCAL test, a homogeneous core sample is assumed, and a one-dimension numerical model is used.

In recent frontier exploration, more and more sandstone reservoirs exhibit complex pore structures. The petrophysical core measurements indicate the complex pore structure. The shape of a primary drainage capillary pressure (Pc) curve is clearly deviated from a power-law function (Figure 1). If such Pc curves are modelled by a single-porosity function, water saturation in the transition zone cannot be properly described. It would result in wrong estimation of the in-place volume and the initial fluid distribution, which then impacts the production forecast. The interpretation with homogeneous assumption could also provide misleading evaluations to the wettability and displacement efficiency.

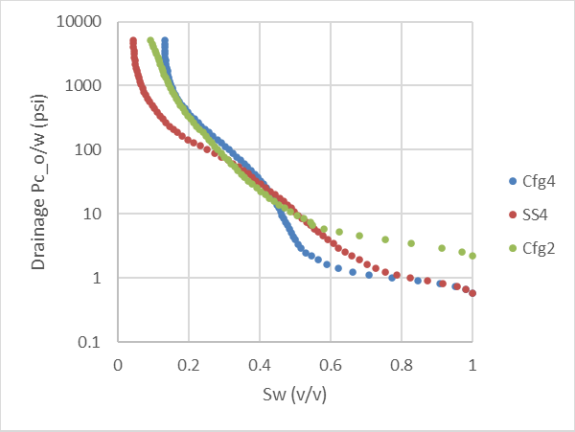

Figure 1. Primary drainage capillary pressure curves measured on the end-trims of a few samples selected in 2018 SCAL program.

For the reservoir in this study, a SCAL program was previously performed and described in 2018 [3]. In the 2018 work, we demonstrated that quality data was obtained with proper design, combination of techniques, and timely QAQC. We also highlighted that the possible impact of the core scale laminations and heterogeneity on the reservoir performance and water cut development requires further investigation.

In literature, many dual-porosity studies have been focused on describing naturally fractured reservoirs where the matrix and fractures are modeled by equivalent medium through a connected-network [4] [5]. This type of dual-porosity model does not describe the formation in this study. On the other hand, most carbonate reservoirs are heterogeneous containing multiple porosity systems. Different data has been used in the heterogeneity characterization and rock typing, including images at different scales, log evaluations, and core measurements.

* Corresponding author: yingxue.wang@shell.conm

Some recent studies can be found in Ref's [6, 7, 8]. Pc and the derived pore throat size distribution have been used in the pore structure characterization and rock typing. Impacts of the heterogeneity on SCAL were studied by both experiments and numerical simulations [9, 10, 11, 12]. On the characterization size, Masalmeh et al. proposed a mathematical formular to describe the Pc with wide range of pore-size distribution [13]. The formular adds a third term, $b\times(S_{w\_cutoff}-S_w)$, to the power-law by Brooks-Corey and Skjaeveland, trying to describe the different shapes of Pc curves. This formular, however, could not describe the measured Pc curves in this study. Moreover, it appears less clear how the parameter b in the Pc formular is linked to other petrophysical measurements. Krause applied the Leverett J-Function on measured Pc curves to represent the sub-core scale capillary heterogeneity [10]. For the pore structures indicated by those drainage Pc curves in Figure 1, J-Function does not improve the characterization.

In this work, we describe a workflow to characterize a Dual Matrix Porosity (DMP) system and derive saturation functions for reservoir models. The paper is organized as follows. In Section 2, we first define the dual matrix porosity using petrophysical and petrographic data. We then describe the method to characterize both the primary drainage and imbibition capillary pressures in Section 3. The Relative permeabilities for dual matrix porosity system is derived in Section 4 using numerical simulations. We discuss the application of DMP approach to reservoir simulations and the uncertainties in Section 5, followed by the conclusions in Section 6.

2 Definition of Dual Matrix Porosity

The reservoir under consideration in this study is represented by aeolian formation. Mineralogy mainly consists of quarts (over 70 wt%) and feldspars, with small amount of calcite, Fe-rich and Mg-rich chlorite clays, which is typical for aeolian formations.

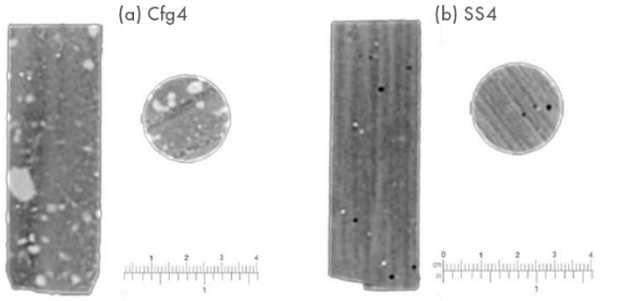

Figure 2. CT images of the core plug samples Cfg4 and SS4 show fine laminations.

The Computed Tomography (CT) scans of a core plug sample show laminations of different thickness from a few millimeters to a few centimeters. Figure 2 are CT images of the core plug samples Cfg4 and SS4, respectively, used in the 2018 SCAL program [3]. The thin sections on the end-trims of those samples further highlight the size-sorted, planar- and cross-laminations (Figure 3). The size-sorted, alternating finer-grained and coarser-grained laminae result in a bimodal grain size distribution. The coarser-grained laminae are composed of well sorted, lower medium sand. And the finer-grained laminae are comprised of very well sorted, lower fine sand. The Scanning Electron Microscope (SEM) images reveal details in pore structure on the end-trim of SS4 (Figure 4). Highly continuous chlorite coating prevents the quartz overgrowths in the formation. In the coarser-grained laminae, the coating is relatively thin and preserves the effect porosity. The left image in Figure 4 illustrates those intergranular pores slightly reduced by the thin chlorite coating. In the finer-grained laminae, thick chlorite coating or filling results in the loss of porosity and increased tortuosity, as shown in the right image in Figure 4.

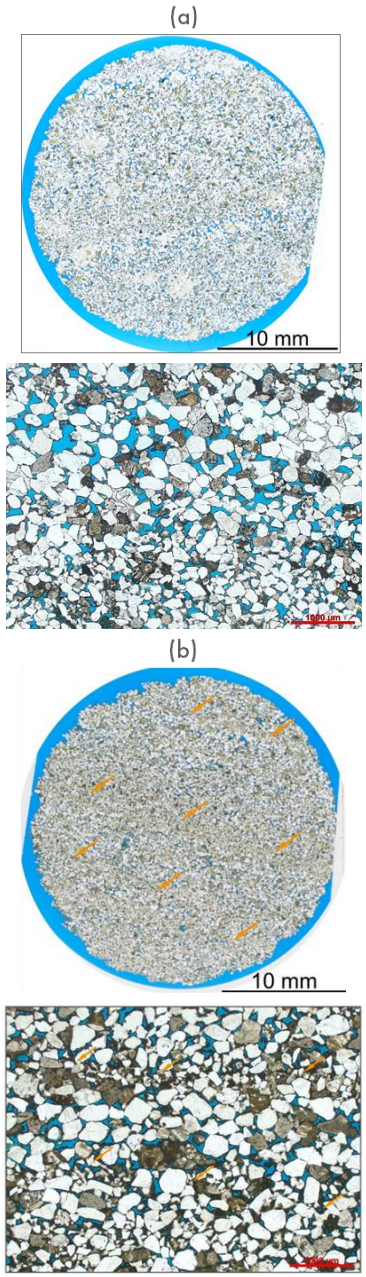

Figure 3. Thin section images of the end-trims of Cfg4 and SS4. Alternating laminae caused by fine and coarse grain sizes can be seen on both samples.

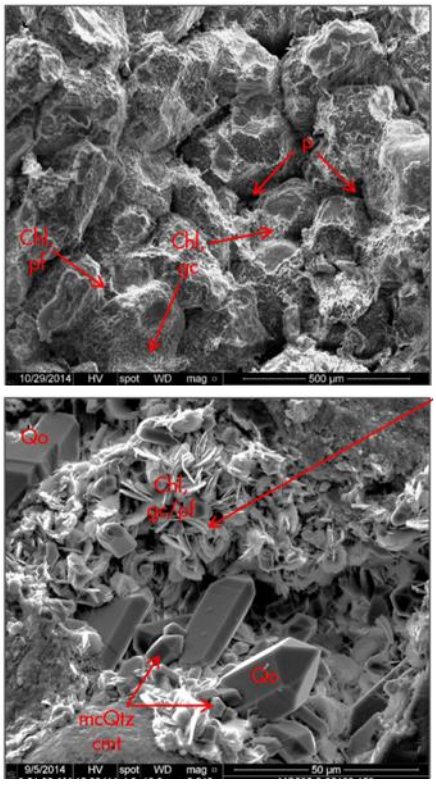

Figure 4. SEM images on the end-trim of SS4. Left: the open pores (p) slightly reduced by the continuous thin chlorite (Chl) coating; right: a magnified view of pores with reduced size due to the grain-coating (gc) to pore filling (pf) chlorite, where Qo marks the sparse quartz overgrowths.

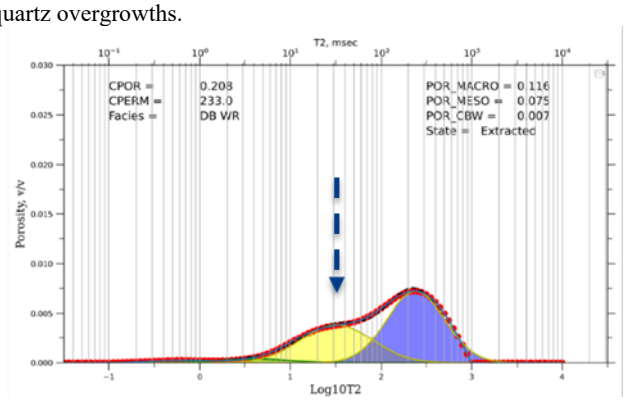

Figure 5. A typical NMR T_2 spectrum, and its Gaussian deconvolution, of a core sample from the reservoir in this study demonstrates the bi-modal pore size distribution. Where the green peak is the T_2 signal of clay bound water, which is not movable and is not used in further analysis. Dashed arrow marks the constant cut-off often used in T_2 evaluation by vendors.

Two matrix porosity systems are defined accordingly: macro- and meso- porosities. The macro-porosity consists larger pores between the coarser grains, which are mostly the primary intergranular pores. Those pores are slightly reduced by the thin grain-coating chlorite, but they are more prominent volumetrically and are the main contributor to permeability. The meso-porosity consists of smaller pores between finer grains and clay-dominated pores. They are more compacted and pervasively cemented by highly microporous, grain-coating to pore-filling chlorite.

The volumetric fraction of each pore system is derived from the Nuclear Magnetic Resonance (NMR) T_2 measurements. Figure 5 is a typical T2 spectrum on the core sample from the reservoir in this study and clearly shows a bi-modal pore distribution. The macro- and meso- porosities are calculated from the T_2 data after Gaussian deconvolution. The arrow in Figure 5 marks the constant T_2 cut-off often used in the petrophysical evaluation. The constant cut-off assumes that both porosity systems have the same permeability [14, 15], which is clearly not the case. Figure 5 shows that the constant T2 cut-off can incorrectly assign part of meso-porosity to macro-porosity. Among the core samples from the reservoir under consideration, the amount of the meso-porosity as a fraction of the total porosity varies from ~0 to 40%. Note that the same Gaussian deconvolution analysis has also been applied to the NMR log, which allows for consistent dual matrix porosity evaluation from core to log scale. Permeability of each porosity system was then estimated using Swanson method [16].

3 DMP Capillary Pressure

3.1 Primary drainage Pc and initialization

The initial water saturation in the reservoir is governed by the primary drainage capillary pressure (Pc), which is often measured by the mercury injection test (ie. MICP), corrected for clay bound water using Hill – Shirley – Klein method [17].

In a mercury capillary pressure test, the actual measured data includes mercury pressure and mercury volume. From measured data, $P_{c,\mathrm{lab}}$ and bulk volume fraction of the non-wetting phase (ie. mercury) BV_{nw} are calculated. BV_{nw} is then fitted to the following function to describe the drainage process in the macro-porosity system, as the nonwetting phase first drains the macro pores.

$$BV_{nw} = 1 - BV_r - BV_w \quad (1)$$

$$BV_w = BV_{wirr} + (1 - BV_r - BV_{wirr})\left(\frac{P_{ce}}{P_c}\right)^{1/N} \quad (2)$$

Where BV_r is the bulk volume fraction of rock grains, BV_{wirr} is the bulk volume fraction of irreducible water, P_{ce} is the capillary entry pressure, and N is the shape factor. The above function is modified from the original Brooks-Corey function using the bulk volume fraction. This is to avoid the non-physical solutions to such parameters as BV_{wirr} and to ensure the total pore volume preserved. Note that the water saturation S_w is a fraction of water volume (V_w) to the pore volume (PV), $S_w = \frac{V_w}{PV} = \frac{BV_w}{\emptyset}$, Eq. (2) can be rewritten as following:

$$BV_{w,\mathrm{M}} = BV_{wirr,\mathrm{M}} + (\emptyset_{\mathrm{M}} - BV_{wirr,\mathrm{M}})\left(\frac{P_{ce,\mathrm{M}}}{P_{c,\mathrm{lab}}}\right)^{1/N_{\mathrm{M}}} \quad (3)$$

Where the porosity ϕ_{M} is the pore volume of the macro system over the total pore volume. Throughout this paper, the capital "M" in the subscript labels the macro-porosity system, the low case "m" labels the meso-porosity system, and the capital "T" refers to the total porosity. Eq. (1) and (3) describe the drainage in the macro-porosity system. Subtracting the $BV_{nw,\mathrm{M}}$ from the total intruded mercury volume BV_{nw} yields the volume fraction occupied by the meso-porosity ($BV_{nw,\mathrm{m}}$). Its drainage capillary pressure can be described by the same

function as Eq. (3) except that a different set of parameters $BV_{wirr,\mathrm{m}}$, ϕ_{m} , $P_{ce,\mathrm{m}}$, and N_{m} are used.

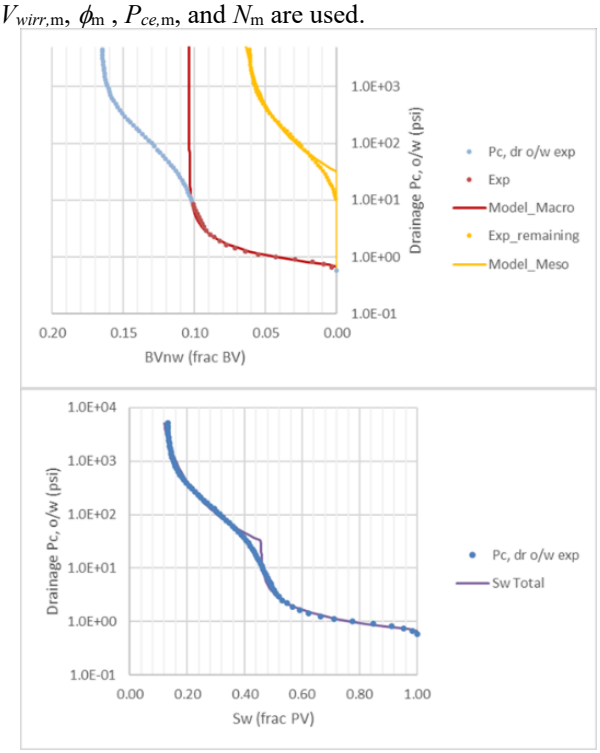

Figure 6. Construction of primary drainage Pc on the end-trim of the sample Cfg4 using DMP approach. See text for explanation.

The MICP curve measured on the end-trim of the sample Cfg4 is used to illustrate the analysis (Figure 6). In the top figure, the light blue dots are the measured Pc converted to the oil-water condition. The red dots mark the portion of the Pc curve fitted to Eq. (3) to derive the parameters for the macro-porosity system: $BV_{wirr,\mathrm{M}}$, $P_{ce,\mathrm{M}}$, and N_{M}. The remaining portion shown in yellow dots is fitted to obtain the corresponding parameters for the meso-porosity system. The total water saturation is calculated as:

$$S_{w,\mathrm{T}} = 1 - \left(BV_{nw,\mathrm{M}} + BV_{nw,\mathrm{m}}\right)\frac{BV}{PV} \qquad (4)$$

where BV and PV are bulk and pore volume of core sample, respectively. The primary drainage Pc using the DMP approach agrees well with the measured data (bottom graph in Figure 6).

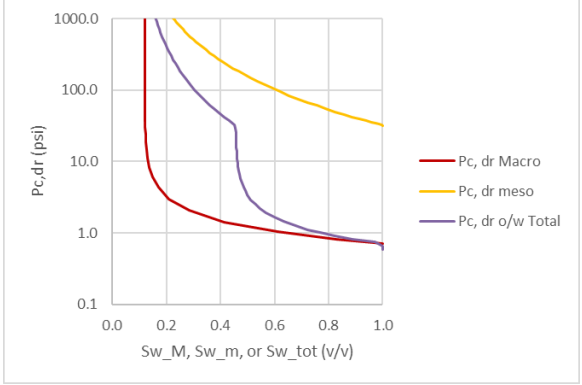

Figure 7. Drainage Pc curves derived from DMP approach, for the sample Cfg4 for macro-, meso- and total porosity system, respectively.

For the sample Cfg4, Figure 7 shows the drainage Pc curves derived from DMP approach for the macro-, meso- and total porosity system, respectively. Note that the saturation S_{w_M}, S_{w_m}, and S_{w_T} is calculated using the corresponding PV of each porosity system. From the figure, at certain maximal capillary pressure ($P_{c,\max}$) achieved in a reservoir (or used in the core preparation), the corresponding water saturation, or the initial water saturation (S_{wi}) is different between macro and meso system. As the macro-porosity system contains larger pores with lower capillary entry pressure, $P_{c,\max}$ is normally high enough such that the $S_{wi,\mathrm{M}}$ is close to the irreducible water saturation $S_{wirr,\mathrm{M}}$. Meso pores are smaller and require much higher entry pressure (~10 to 100 times) for oil to enter the pores. The meso-porosity is partially saturated with oil at the end of the drainage process; $S_{wi,\mathrm{m}}$ is often higher than $S_{wi,\mathrm{M}}$.

3.2 Imbibition Pc and residual oil saturation

To model the displacement properly, we need to evaluate the wettability condition and the possible ranges of residual oil saturations (S_{or}) for each porosity system. The imbibition Pc curves provide such evaluation.

In Section 3.1, the primary drainage Pc is characterized by two porosity systems. At the end of the drainage, the initial oil saturation (S_{oi}) is different in each porosity system. Consequently, wettability could vary between two porosity systems. The imbibition curve P_c^{imb} is converted from the primary drainage curve P_c^{dra} as shown below for each pore system, following the approach by Masalmeh and Jing [18]

$$P_c^{\mathrm{imb}}\left(S_w^{\mathrm{imb}}\right) =$$

$$P_c^{\mathrm{dra}}\left(1 - S_w^{\mathrm{dra}} + S_{wirr} + S_{wt} - S_{ot}\right) \cdot \frac{\cos\left(\theta_{\mathrm{imb}}\right)}{\cos\left(\theta_{\mathrm{dra}}\right)} \qquad (5)$$

Where θ_{imb} and θ_{dra} are the imbibition and drainage contact angles, respectively. In this work, we used $\theta_{\mathrm{dra}} = 30°$, as post-cleaning core samples were water-wet during primary drainage. S_{wt} represents either trapped water during drainage or the difference between the S_{wc} and the S_{wi} when the imbibition experiment starts. S_{ot} is the linear interpolation between zero and the maximal trapped oil $S_{ot,\max}$:

$$S_{ot} = S_{ot,\max} \cdot \frac{1 - S_w^{\mathrm{dra}}}{1 - S_{wirr}} \qquad (6)$$

This approach assumes that there is no spontaneous imbibition, which was the case for the core samples evaluated in this study [3]. Besides, the conversion uses one constant contact angle to represent wettability. Actual wettability may vary among different pores. In this study, we use two constant contact angles to represent the wettability for macro- and meso-porosities, respectively. Comparison to the imbibition Pc from centrifuge tests suggest that the wettability difference between two porosity systems has larger impact and any possible wettability variations in each porosity system appears to be secondary.

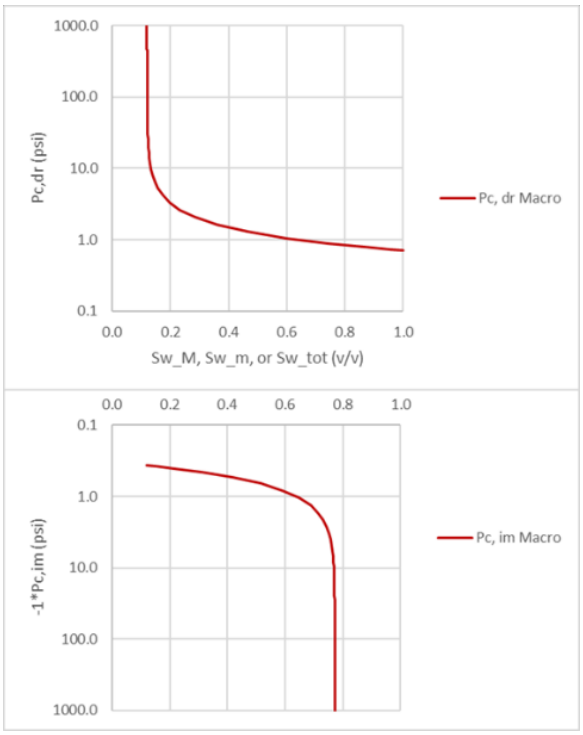

Figure 8. Calculation of the imbibition Pc (bottom) form the primary drainage curve (top) for the macro-porosity system. Note that the imbibition Pc has been multiplied by -1 to be displayed in log scale, same for figures below.

For the macro-porosity, S_w at the beginning of the imbibition is at $S_{wirr,M}$, so $S_{wt} = 0$. Figure 8 shows the derivation of the macro imbibition Pc from drainage Pc derived in Sec. 3.1 (Figure 7). Note that in the figure, log scale has been used to illustrate the details at low Pc values and the imbibition Pc has been multiplied by -1. For the meso-porosity as shown in Figure 9, a bounding imbibition Pc curve is first constructed from its corresponding drainage Pc (Figure 7) following similar procedure as that for the macro-porosity system. In the next, the scanning imbibition Pc curve at $S_{wi,m} > S_{wirr,m}$ is calculated by scaling the saturation ranges accordingly. For the bounding imbibition Pc curve, S_w varies from S_{wirr} to 1-$S_{ot,max}$; and for the scanning Pc curve, S_w varies from S_{wi} to 1-S_{ot}.

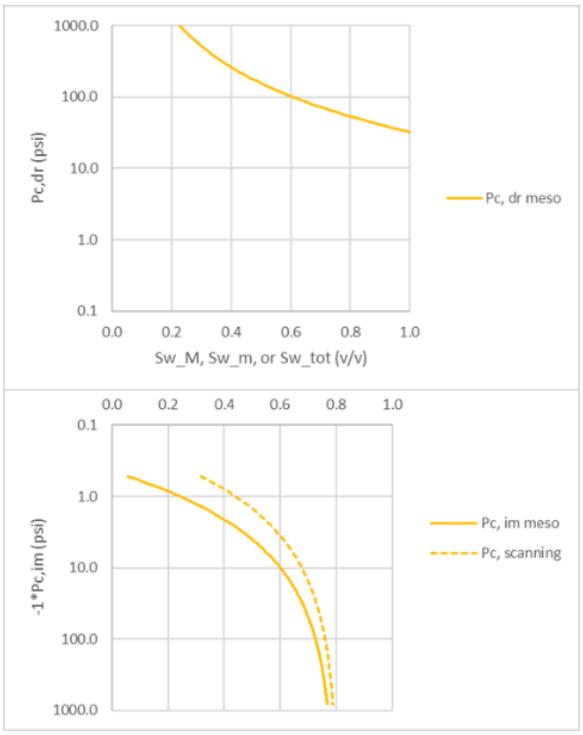

Figure 9. Calculation of the imbibition Pc (bottom) from the primary drainage curve (top) for the meso-porosity system. In the bottom graph, solid line is the bounding imbibition curve, and the dashed line is the scanning curve.

The trapped (or residual) oil saturation S_{ot} for each pore system depends on its initial oil saturation S_{oi}. Here, we use the Land's correlation [19] to model the initial-residual (IR) relationship:

$$S_{ot} = \frac{S_{oi}}{1+C \cdot S_{oi}} \tag{7}$$

The Land's coefficient C is defined using the S_{or} data from SCAL test to capture the impacts from wettability as well as uncertainties in core samples. The Land's correlation was originally proposed to describe the residual gas in the transition zone for a water-wet reservoir. We apply this correlation to an oil reservoir assuming that the reservoir wettability has not been modified to very oil-wet situation and the oil trapping is still largely impacted by the sorting and pore structure. Based on regional SCAL data, we think it is a reasonable assumption.

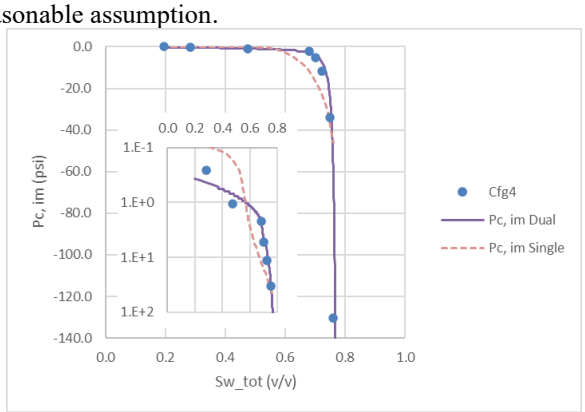

Figure 10. Comparison of dual porosity imbibition Pc curves and those measured by centrifuge on the samples Cfg4, where the inserted figure plots -1*Pc in log scale to show the matching details at the lower Pc region.

Table 1. Pc Parameters for Cfg4

Porosity System	Pore System	Prim. Dra.	Imb.
Macro	P_{ce} (psi)	0.71	-0.37
	N (dimensionless)	0.630	0.630
	S_{wi} (v/v)	0.12	0.12
	S_{ot} (v/v)	0	0.228
Meso	P_{ce} (psi)	32.19	-0.53
	N (dimensionless)	2.202	2.202
	S_{wi} (v/v)	0.02	0.32
	S_{ot} (v/v)	0	0.212

The imbibition Pc curve on a core plug sample is constructed as follows. First, an array of imbibition Pc values are generated. Secondly the water saturation S_w in each porosity is determined at a certain given Pc value. S_w remains at S_{wi} if the given Pc is less negative than P_{ce}^{imb}; Pc does not reach the entry yet. Total saturation is calculated as

$$S_{w,\text{T}} = \frac{S_{w,\text{M}}.\emptyset_{\text{M}} + S_{w,\text{m}}.\emptyset_{\text{m}}}{\emptyset_{\text{T}}} \quad (8)$$

The derived imbibition Pc curve on the total porosity is then constrained to the imbibition Pc curve measured by centrifuge technique on the core plug. By fitting the Pc curve to the experimental data, the following parameters are varied: contact angles for macro- and meso- porosities, respectively, and the Land's coefficient. Figure 10 compares the dual porosity imbibition Pc (solid line) with that measured on the sample Cfg4. The relevant Pc parameters are listed in Table 1. The dual porosity approach can reasonably describe the measured Pc. For the group of core samples where imbibition Pc was measured, we obtain the contact angles of 100° - 130° for the macro porosity and < 100° for the meso-porosity. The derived contact angle ranges suggest that the macro-porosity system has more oil-wet tendency, and the meso-porosity appears neutral wet. We will further assess the wettability condition in two porosity systems in the next subsection. Moreover, the fitting results suggest that the S_{or}'s in both porosity systems can be calculated by a same Land's coefficient; and the coefficient varies between 2.8 and 3.8 for most samples. Note that different combination of the macro and meso contact angles may yield similar fitting results to the centrifuge imbibition Pc. In Sec. 4, we further evaluated the uncertainty ranges in the contact angles.

Also shown in the figure is an imbibition curve (dashed line) calculated from drainage curve assuming simple porosity and uniform wettability (i.e. contact angle). In comparison, the approach with simple porosity and uniform wettability appears over simplified and cannot describe the measured data.

4 DMP Relative Permeability

4.1 Numerical model

With different pore structure and wettability conditions in macro- and meso-porosity systems, one can expect different displacement characteristics or relative permeabilities (Kr) in two systems. To evaluate the oil-water displacement, we built a three-dimensional numerical model in MoReS, a Shell proprietary reservoir simulator. The model was in cylindrical shape with core plug's diameter and length honored. The number of grid blocks in the x, y, and z directions was 26, 26, and 32, respectively. The injection was along the z direction. The first and last grid blocks in the z direction were not part of the core but are used to implement the injection and production constraints to mimic the actual core flooding test. At the injection side (z = 1), a constant flux boundary condition was imposed following the same ratio of injection rates in the flooding tests. At the production size (z = 32), a constant pressure (200 psi) boundary was imposed.

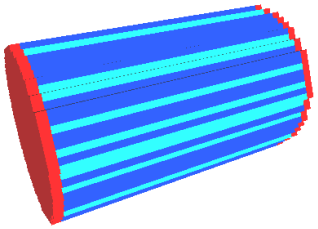

Figure 11: A three-dimensional numerical grid used in simulations; porosity variations were shown.

Table 2. Base Properties of the Core Sample SS4

Plug ID	SS4
Length (cm)	4.049
Diameter (cm)	2.529
Total Porosity (v/v)	0.217
Macro Porosity (v/v)	0.137
Meso Porosity (v/v)	0.080
Permeability to Brine (mD)	149

The core sample dimensions, and base properties were from measurements. In this session, we use the data from the sample SS4 for discussion purpose and its numerical model is illustrated in Figure 11. Table 1 summarizes the properties of the sample SS4. The macro- and meso- porosities were directly modelled as laminated layers along the flow direction. The colors in Figure 11 indicates porosity variations in the plug: the dark and light blue bocks are macro- and meso- porosity, respectively, and the red grid blocks at both sides are end-pieces. This conceptual model is consistent with the CT scan images on the core plug). The configuration of those laminated layers was randomly generated.

4.2 SCAL inputs and AHM variables

A steady state flooding test was performed on this 3D numerical model following the same injection schedule as that used in the core test in 2018. The simulated delta pressure was compared with that measured. An Assisted History Match (AHM) workflow was deployed to explore the solution space in the following parameters for each porosity system: absolute permeability, imbibition Pc, and relative permeability.

The model was initialized using primary drainage Pc curve. The primary drainage Pc curve measured on the end-

trim of the same plug (SS4) was analyzed using the method in Sec. 3.1. Table 2 lists the relevant fitting parameters. For each porosity system, its primary drainage Pc curve was used to calculate the corresponding S_{wi} at the Pc value used during core initialization. The numerical model was then initialized with the above S_{wi}'s values for each pore systems. This ensured the hydrostatic equilibrium at the initialization. In the experiment, the sample SS4 was initialized with a $P_{c,\max}$ of 200 psi and the total S_{wi} on the core plug was 0.15. Corresponding S_{wi} was 0.01 and 0.39 for macro- and meso-porosity, respectively. In the experiment, the sample was initialized by porous plate and its saturation was carefully checked both through volumetric and by weight. In the simulation, we assigned constant and uniform saturations in each grid.

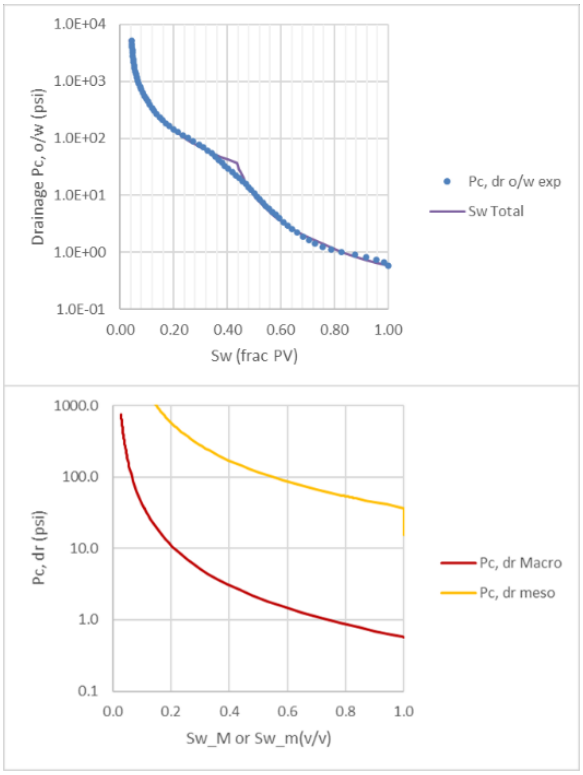

Figure 12. Primary drainage Pc curve on the sample SS4. Top graph compares the dual porosity Pc with the measured data; bottom graph shows the Pc curves for the macro and meso porosity systems, respectively.

Table 3. Pc Parameters for SS4

Porosity System	Pore System	SS4 End-trim
Macro	P_{ce} (psi)	0.58
	N (dimensionless)	1.794
	BV_{wirr} (v/v)	0.0014
	S_{wirr} (v/v)	0.01
Meso	P_{ce} (psi)	37.46
	N (dimensionless)	1.563
	BV_{wirr} (v/v)	0.0026
	S_{wirr} (v/v)	0.03

The macro absolute permeability is expected to be high and closer to that measured on the core plugs. In the AHM, macro permeability was varied linearly between pre-defined low and high values. The meso permeability was modelled through a power law poro-perm correlation: $K = 13632.6\phi^{\beta}$, based on the Swanson estimation mentioned in Sec. 2. In AHM the meso permeability was varied via the power β to access its uncertainties.

The imbibition Pc measurement on the same plug was not available. The following Brooks-Corey function was used to model the imbibition Pc for each porosity system.

$$P_c = P_{ce} \cdot \left[\frac{1-W}{S_{norm}{}^{N}} - \frac{W}{(1-S_{norm})^{N}}\right] \quad (5)$$

In the original definition, W is the wettability index. and can be estimated from USBM index (w) as $W = 0.5*(1-w)$. In this work, we mainly used this parameter to vary the amount of spontaneous imbibition in the Pc curve. Core measurement showed hardly any spontaneous imbibition. Therefore, in the AHM, W was only varied over a narrow range to void excessive spontaneous imbibition. S_{norm} is the normalized saturation:

$$S_{norm} = \frac{S_w - S_{wirr}}{1 - S_{orw} - S_{wirr}} \quad (6)$$

The S_{wirr} and the shape factor N were from the primary drainage Pc for both macro- and meso- porosities (Table 2). The residual oil saturation S_{orw} was constrained to the average value measured by centrifuge on the core samples with similar permeability and porosity. The capillary entry pressure P_{ce} for the imbibition was calculated from drainage as:

$$P_{ce}^{imb} = P_{ce}^{dra} \cdot \frac{\cos\theta_{imb}}{\cos\theta_{dra}} \quad (7)$$

The $P_{ce}{}^{dra}$ was from the dual porosity analysis on the measured data and was relatively certain. As mentioned in Sec. 3.2, $\theta_{\text{dra}} = 30°$ was used. The variation in $P_{ce}{}^{imb}$ was mainly driven by the imbibition contact angle, i.e. the wettability change. Based on the imbibition Pc analysis in Sec. 3.2, in the AHM, the contact angle was varied between 92° and 120° for the macro- porosity, and between 90° and 92.5° for the meso-porosity. In addition, the meso wettability index was varied to allow small amount of spontaneous imbibition.

Table 4. Variables and Their Ranges used in the AHM

Groups	Parameters	Low	High
Absolute Permeability	$K_{abs,M}$ (mD)	100	320
	$K_{abs,m}$ (mD)	0.01	10.1
Imbibition Pc and Wettability	$P_{ce,M}{}^{Imb}$ (psi)	-0.335	-0.029
	θ_M	*120°*	*92°*
	$P_{ce,m}{}^{Imb}$ (psi)	-1.885	-0.036
	θ_m	*92.5°*	*90.0°*
	W_m	0.85	0.99
Bounding Drainage kr	$n_{w,M}{}^{dra}$	3	4.5
	$n_{w,m}{}^{dra}$	3	5
	$n_{o,M}{}^{dra}$	2.5	4
	$n_{o,m}{}^{dra}$	1.5	3.5

	$k^0_{ro,\mathrm{M}}$	0.5	1
	$k^0_{ro,\mathrm{m}}$	0.5	1
Bounding Imbibition kr	$n_{w,\mathrm{M}}{}^{\mathrm{imb}}$	1.5	3
	$n_{w,\mathrm{m}}{}^{\mathrm{imb}}$	3.5	5.5
	$n_{o,\mathrm{M}}{}^{\mathrm{imb}}$	3	5
	$n_{o,\mathrm{m}}{}^{\mathrm{imb}}$	1.5	3.5
	$k^0_{rw,\mathrm{M}}$	0.3	0.7
	$k^0_{rw,\mathrm{m}}$	0.05	0.5

Corey functions were used to describe the bounding relative permeability in each porosity system.

$$k_{rw}(S_w) = k^0_{rw} \cdot \left(\frac{S_w - S_{wirr}}{1 - S_{wirr} - S_{orw}}\right)^{n_w} \quad (6)$$

$$k_{ro}(S_w) = k^0_{ro} \cdot \left(\frac{1 - S_w - S_{orw}}{1 - S_{wirr} - S_{orw}}\right)^{n_o} \quad (7)$$

Where k^0_{rw} and k^0_{ro} are the end-point relative permeabilities for water and oil, respectively; n_w and n_o are the Corey exponents. S_{wirr} and S_{orw} are defined in the capillary pressure functions. In the AHM, k^0_{rw}, k^0_{ro}, n_w, and n_o for each porosity system were varied over the ranges reflecting the wettability conditions. In the above functions, the saturation S_w was defined in each porosity system itself. The relative permeability was normalized to the absolute permeability of its own porosity system. In the meso-porosity system, S_{wi} was higher than $S_{wirr,\mathrm{m}}$; the pores were partially drained at the beginning of imbibition. Oil relative permeability was described by the scanning curves using a hysteresis model modified from the original Killough model [20, 21]. The modification was to ensure the scanning curves are properly bounded by their bounding curves. Water relative permeability was assumed to be the same between the primary drainage and imbibition processes. Given that the meso-porosity does not show oil-wet tendency as shown in Sec. 3.2, we think that the hysteresis effect in water phase can be ignored.

In the AHM, k^0_{rw}, k^0_{ro}, n_w, and n_o for each porosity system were varied over the ranges reflecting the wettability conditions. Table 3 summarizes the AHM variables and their ranges.

4.3 Results

The matching objective functions were the delta pressures during the steady state flooding test on the sample SS4. To increase the robustness, saturation distributions (or profiles if available) should be included as objective function as well. The AHM used both Monte Carlo (MC) and Markov-chain Monte Carlo (MCMC) solvers to achieve better matches to the objective function and analyzed variable uncertainties within the prescribed ranges. An example of the final match to the measured delta pressure is shown in Figure 13. The saturation change along the plug at different times during the injection are highlighted in Figure 14.

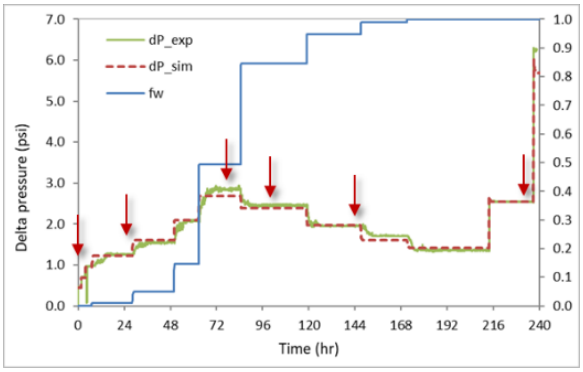

Figure 13. Simulated delta pressure (dP_sim, red dashed line) match to the measured data (dP_exp, green solid line). Where blue line is the water fractional flow (fw) to show the injection schedule and the red arrows mark the time step of those saturation maps shown in Figure 14.

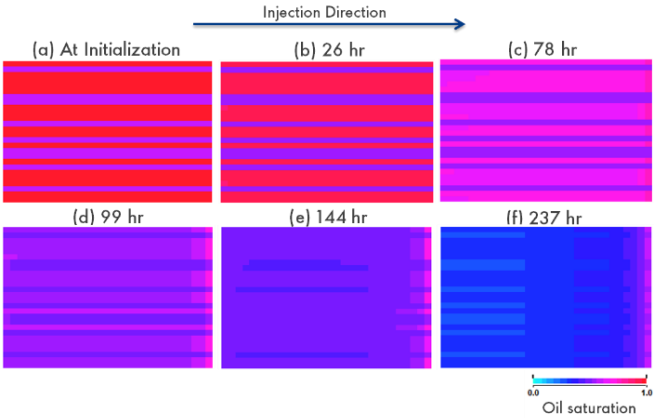

Figure 14. Oil saturation distribution along the core plug at different times of the injection as marked in Figure 13.

In the simulation, the co-injection of oil and water started at around 7 hr. And the water and oil were co-injected at the following ratios: 0, 0.01, 0.05, 0.15, 0.50, 0.85, 0.95, 0.99, and 1. Figure 14 (b) is the saturation map near the end of the injection at the ratio of 0.01. Compared with Figure 14 (a), the subtle color change in the meso-porosity indicated that the water entered the meso-porosity. This could be due to the spontaneous imbibition as indicated by the small portion of the positive imbibition Pc for the meso-porosity in the bottom graph of the Figure 15. As the injection continued, for the water-oil ratios between 0.05 and 0.99, the macro-porosity showed larger saturation changes as illustrated in Figure 14 (c) to (e). The macro-porosity appeared to be the main contributor to the flow. The bump flood towards the end of the injection that started at ~214 hr improved the displacement in both porosity systems. In Figure 14 (f), both macro- and meso- porosities were flooded.

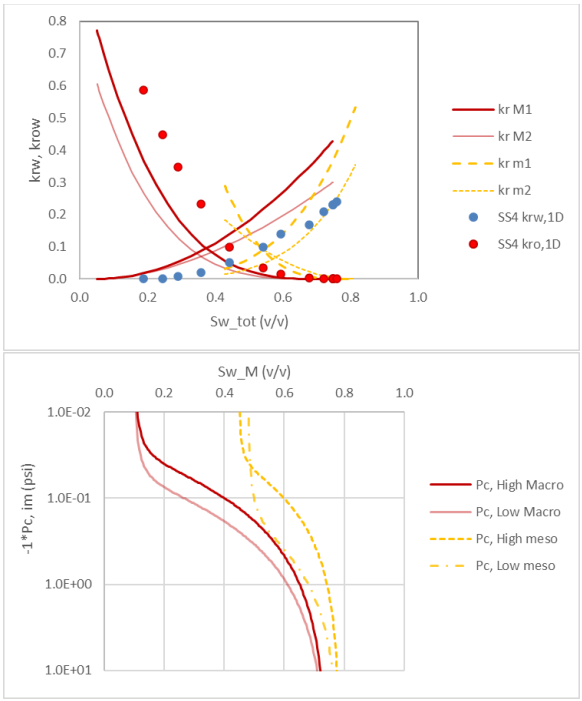

Figure 15. Example macro and meso relative permeability (top) and imbibition Pc (bottom) curves from the AHM that match the delta pressure of SS4. Where red lines illustrate the possible solution ranges for the macro-porosity and yellow lines are scanning curves for the meso-porosity. See text for explanation.

The AHM provided solutions to the relative permeability and imbibition Pc for each porosity system. Two sets of Kr and Pc curves are plotted in Figure 15 to illustrate possible solutions. Overall, solutions to the macro-porosity Pc and Kr were better constrained compared to those for the meso-porosity. Besides, drainage P_{ce} of two porosity systems differed more than an order of magnitude; their imbibition P_{ce} became much closer. It suggested that the contact angle of the macro-porosity was higher than that of the meso-porosity. Also shown in the figure is the relative permeability using one-dimensional simulation assuming homogeneous core sample. In comparison, relative permeability from 1D interpretation fell in between the macro and meso results and did not reflect the wettability conditions in the core sample.

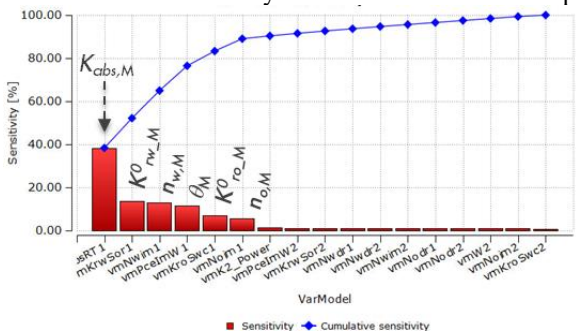

Figure 16. Sensitivity of the variables in the AHM, where the top impacting variables are labeled. See text for explanation.

Sensitivities among AHM variables (Figure 16) highlighted the top impacting variables in the pressure match. The macro absolute permeability ($K_{abs,M}$) had the highest impact. The next five impacting variables were $k^0_{rw,M}$, $n_{w,M}$, θ_M $k^0_{ro,M}$, $n_{w,M}$, and $n_{o,M}$, respectively. This is consistent with the observation based on the saturation change that macro-porosity was the main contributor to the flow. The rest variables accounted for ~10% of the cumulative sensitivity.

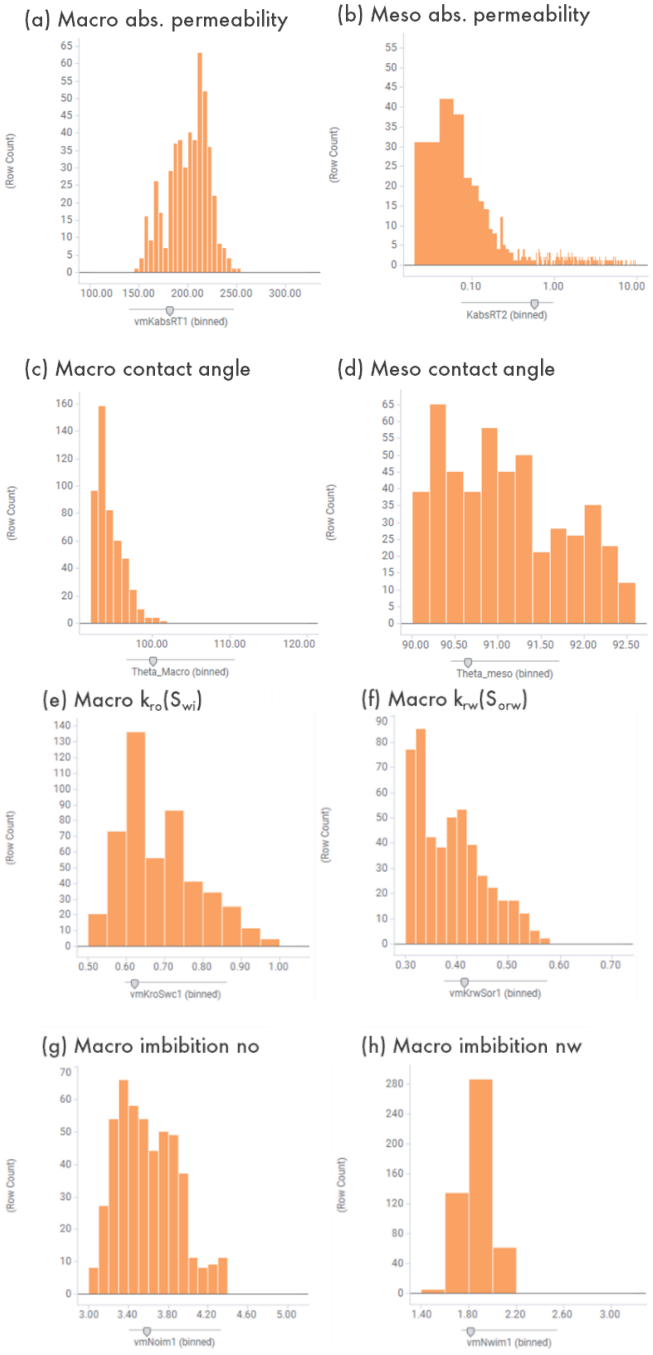

Figure 17. Histograms of selected parameter ranges where the solutions were found by AHM. See text for explanation.

AHM evaluated the convergence of those history matching variables in the solution space. Strong convergence generally suggests that the parameter is well constrained. Among those variables used in AHM (Table 4), different degrees of convergence were observed on eight of them. Figure 17 summarizes the ranges of those eight parameters where the delta pressure could be matched, including absolute permeabilities and contact angles of both porosity systems, end-point relative permeabilities, and Corey exponents of the macro-porosity system. The macro absolute permeability

converged around 200 mD; the meso permeability was much lower, varying between 0.04 and 0.4 mD. The contact angle for the macro-porosity converged around 92° to 100°. For the meso-porosity, the contact angle did not clearly converge; solutions were possible between ~90° and 92°. This result suggested that the macro-porosity was slightly more oil-wet compared with the meso-porosity, which was consistent with the imbibition Pc analysis in Sec. 3.2. Among those Corey parameters varied in the AHM, macro oil end-point relative permeability $k^0_{ro,\mathrm{M}}$ was found centered around 0.55 and 0.75, while meso $k^0_{ro,\mathrm{m}}$ varied between 0.3 and 0.55. Imbibition oil Corey exponent for the macro porosity $n_{o,\mathrm{M}}^{\mathrm{imb}}$ was 3.2 to 4.0. And the water Corey exponent for the meso porosity $n_{w,\mathrm{m}}^{\mathrm{imb}}$ was around 2.0.

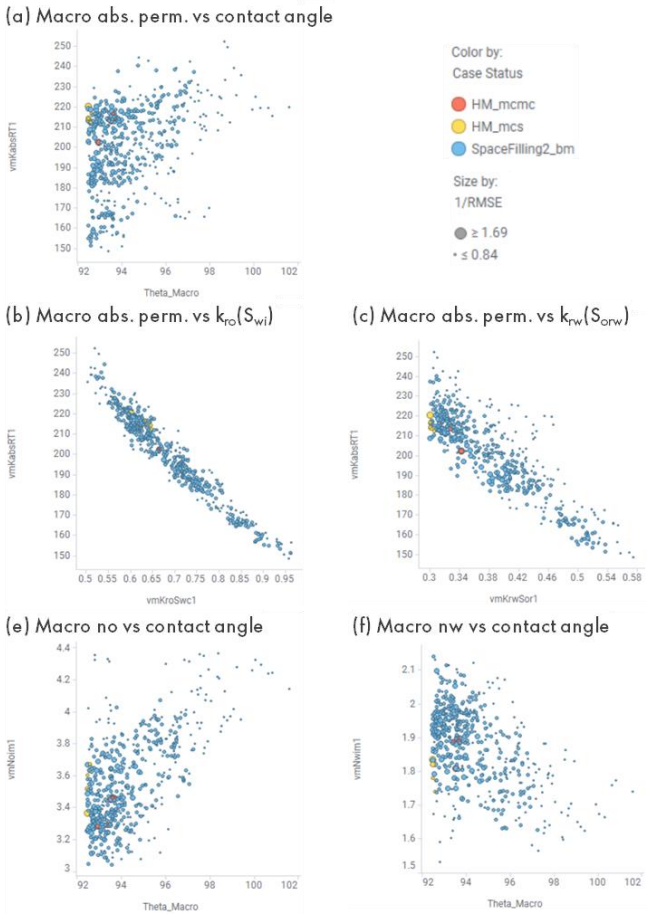

Figure 18. Cross-correlations between AHM variables. See text for explanation.

Cross-correlations among fitting parameters were also reviewed (Figure 18). In the figure, the blue dots are all cases created by AHM using a proxy. Red and yellow dots are top history matched cases after MC and MCMC optimization. The dot size is inversely proportional to the Root Mean Square Error (RMSE) per case: the larger the dot size, the smaller the matching error. From Figure 18 (a), the macro contact angle appeared to be weakly correlated to the macro absolute permeability: the higher the permeability, the higher the contact angle. For macro-porosity system in the reservoir in this study, we generally observed the lower values of $P_{ce,\mathrm{M}}$, $S_{wirr,\mathrm{M}}$, and N_{M} (i.e. better sorting), as its absolute permeability increases. In other word, at certain $P_{c,\max}$, higher oil saturation can be achieved with increased absolute permeability. Consequently, the wettability in the macro porosity is more likely to be altered away from the original water-wet condition. In Figure 18 (b) and (c), the end-point relative permeabilities for macro-porosity $k^0_{ro,\mathrm{M}}$ and $k^0_{rw,\mathrm{M}}$ were strongly correlated with the absolute permeability $K_{abs,\mathrm{M}}$. For the oil-water flow simulations, what really matters are the the effective permeabilities, i.e. K_{abs}* $k^0_{ro,\mathrm{M}}$ and K_{abs}* $k^0_{rw,\mathrm{M}}$. Figure 18 (d) and (e) suggested weak correlations between macro Corey exponents, n_o and n_w, and the contact angle. As the contact angle increases in the macro-porosity, the pores become more oil wet. The increase in n_o and the decrease in n_w reflect the impact of wettability change on the relative permeability curvatures.

It worth noting that the above simulations were based on one layering configuration randomly generated. We repeated the simulations with another layering configuration, using the same set of history matched parameters. And the delta pressure was still matched.

5 Application to Reservoir Simulations

5.1 Model initialization

In Sections 3 and 4, we have used the specific core samples Cfg4 and SS4 to illustrate the workflow the characterize the dual matrix porosities and evaluate the flow properties. In this section, we discuss a few key points when applying the DMP SCAL in reservoir modeling and simulations.

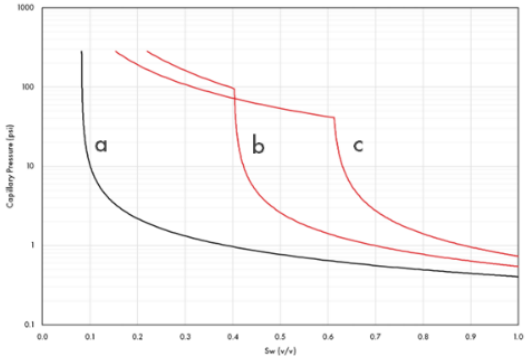

Figure 19: Comparison of Pc curves with same total porosity but varying fraction of meso-porosity. See text for explanation.

Primary drainage Pc is often used to initialize a reservoir model. In a reservoir with dual matrix porosities, Pc shape could vary widely as the amount of the meso-porosity changes. Figure 19 displays three Pc curves used to model the reservoir under consideration. All three Pc curves have the same total porosity of 0.21 but different amount of the meso-porosities. The curve “a” has the least amount of meso-porosity; 7% of the total porosity in this case. The meso entry pressure $P_{ce,\mathrm{m}}$ is higher than 200 psi, below which the Pc curve is the same as a single porosity case. The curves “b” and “c” have 40% and 60% of meso-porosities, respectively. As the meso-porosity increases, it accounts more in saturation. Although $P_{ce,\mathrm{m}}$ is slightly reduced, the meso Pc still dictate the initial water saturation S_{wi}. For the reservoir we study, in situ $P_{c,\max}$ is around 200 psi. The meso-porosity is partially filled with oil. A single porosity approach would result in wrong in-place volume estimate. As illustrated in Figure 20, either S_o in the meso-porosity is over estimated (left graph), or the S_{wi} is over estimated (right graph).

5.2 Flow and relative permeability

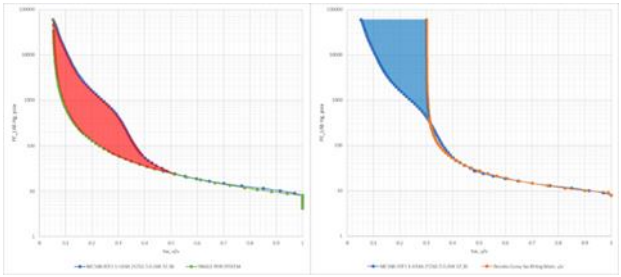

Figure 20. Illustration of a Pc with dual porosity feature characterized by simple porosity functions (Brooks-Corey). See text for explanation.

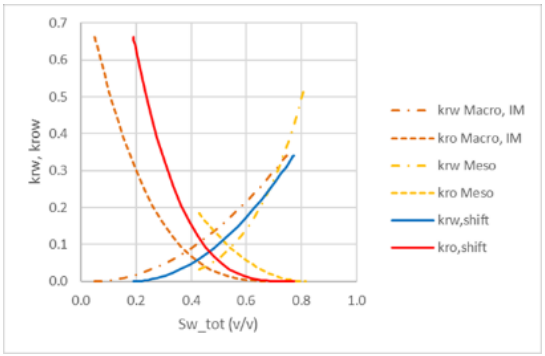

Figure 21. Simplified relative permeability curves (solid lines) used in reservoir simulations. See text for explanation.

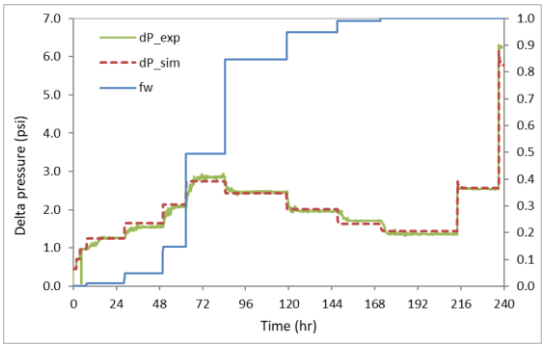

Figure 22. Delta pressure match using a homogenized model with average properties. See text for explanation.

In reservoir simulations, it is desired to simplify the relative permeability inputs but still properly describe the displacement. From the core scale simulations, meso absolute permeability is about three to four orders of magnitude lower than the macro's. The flow from the meso-porosity is very limited. Based on this learning, we constructed the relative permeability assuming that the meso-porosity accounts for the saturation, but only macro-porosity contributes to the flow. As shown in Figure 21, a new set of relative permeability curves for the sample SS4 (solid lines) were derived using the macro relative permeability values but shifting the saturation to account for the meso-porosity. To verify this simplification, we homogenized the numerical model (Figure 11) with constant porosity, permeability, and initial saturation, and simulated the steady state flood again. Those properties were volumetrically averaged between two porosity systems. Simulated delta pressure reasonably matched the measured data (Figure 22).

The robustness of this simplification approach was further tested with meso-porosity accounts for 50% of the total porosity. Following the same workflow, we first generated the delta pressure by simulating a steady state test on the 3D numerical core. This delta pressure was matched by the simplified relative permeability on the homogenous core.

5.3 Uncertainties and future work

In this work, pore structure is characterized by two distinct porosity systems. Both NMR T2 and MICP indicate continuous pore size distribution. When the pore size changes are gradual with long capillary transition zone, this dual porosity approach may not accurately describe the pore structure. Both the primary drainage and imbibition Pc curves could be over simplified, result in uncertainties in S_{wi} and S_{orw} estimations. Moreover, in the imbibition Pc characterization, uniform wettability is assumed in each porosity system by using constant contact angles. In the scenarios of large transition zones, S_{wi} varies in different pores, a constant contact angle that matches the imbibition Pc at high S_w may be too high for those large pores at low Sw. The wettability of those large pores may be overestimated.

When preparing the saturation functions for the reservoir simulations, we have simplified the relative permeability by assuming that meso-porosity contributes to the initial saturation but does not actively contribute to the flow. This is due to laminated structure in the aeolian formation and the large permeability contrast between two porosity systems. In the field, with large draw-down and/or pressure depletion, flow from the meso-porosity may require further evaluation.

In other formations where the meso-porosity is embedded in the macro-porosity system and randomly distributed, the dual matrix porosity approach presented in this work is still applicable. However, the macro- and meso- porosities are interacting with each other; the flow from the meso-porosity can be collected in the macro matrix. In this case, meso-porosity not only affects the saturation but also impacts the flow. The detailed study combining core measurements and simulations are ongoing.

6 Conclusions

In this work, we presented a workflow to characterize the saturation functions for a dual matrix porosity system with the combination of analytical analysis and numerical simulations. Some key conclusions from this study are listed below.

- Alternating size-sorted laminations result in a dual matrix porosity system. Each porosity has distinct pore structures because of the gain size and clay distributions.
- The meso-porosity can be (partially) saturated with oil with high enough in situ Pc. A dual matrix porosity Pc is required to properly estimate the initial in-place hydrocarbon volume and its distribution.
- Imbibition Pc provides assessment of wettability conditions in each porosity system. The macro-

porosity appears to be further modified away from the water wet condition compared with the meso-porosity.

- The meso-porosity may remain weakly water wet if the water saturation is high. Spontaneous imbibition could contribute to the flow at lower Sw. But the overall flow contribution of the meso-porosity is limited due to the large contrast in absolute permeabilities between two systems.
- In reservoir simulations, relative permeability of a dual matrix porosity system may be simplified by accounting the meso-porosity in saturation only.

We would like to thank Menno Hartemink, Jeffery Calhoun, Marzena Jaminski, and Mike Hawkins for insightful discussion and help in AHM.

Reference

[1] J. Thomeer, "Introduction of a Pore Geometrical Factor Defined by the Capillary Pressure Curve," *J Pet. Tech.,* vol. **12**, no. 3 (1960)

[2] R. Brooks and A. Corey, "Hydraulic properties of porous media," *Hydrology Paper,* vol. **3** (1964)

[3] Y.-X. Wang and S. Masalmeh, "Obtaining High Quality SCAL Data: Combininig Different Techniques, Saturation Monitoring, Numerical Interpretation and Continuous Monitoring of Experimental Data," in *The International Symposium of the Socienty of Core Analysts*, Trondheim (2018)

[4] F. Kuchuk, D. Biryukov and T. Fitzpatrick, "Fractured-Reservoir Modeling and Interpretation," SPE 176030 (2015)

[5] M. Raslan, A. Gupta, H. Ates and K. Jessen, "Upscaling of Discrete Fracture Characterization to Dual-Porosity Models Using an Advanced Transfer Function," in *the Middle East Oil, Gas and Geoscience Show*, Manama (2023)

[6] M. Dernaika, B. Mansour, D. Gonzalez, S. Koronfol, F. Mahgoub, O. Jallad and M. Contreras, "Upscaled Permeability and Rock Types in a Heterogeneous Carbonate Core from the Middle East," in *SPE Reservoir Characterization and Simulation Conference and Exhibition*, Abu Dhabi (2017)

[7] M. Dernaika, M. Sahib, D. Gonzalez, B. Mansour, O. Jallad, S. Koronfol, G. Sinclair and A. Kayali, "Core Characterization and Numerical Flow Simulation in Representative Rock Types of the Raudhatain Field in Kuwait," in *SPE Kuwait Oil & Gas Show and Conference*, Kuwait City (2017)

[8] L. Rojas, A. Tveritnev and C. Pinillos, "Rock Type Characterization Methodology for Dynamic Reservoir Modelling of a Highly Heterogeneous Carbonate Reservoir," in *Abu Dhabi International Petroleum Exhibition & Conference*, Abu Dhabi (2020)

[9] S. Masalmeh, "The effect of wettability heterogeneity on capillary pressure and relative permeability," *J Pet Sci & Eng,* vol. **39** (2003)

[10] M. Krause, "Modeling and Investigation of the Influence of Capillary Heterogeneity on Relative Permeability," in *SPE Annual Technical Conference and Exhibition*, San Antonio (2012)

[11] F. Nono, H. Bertin and G. Hamon, "An Experimental Investigation of the Oil Recovery in the Transition Zone of Carbonate Reservoirs Taking Into Account Wettability Change," in *International Petroleum Technology conference*, Doha, Qatar (2014)

[12] G. Zhang, S. Foroughi, A. B. M. Raeini and B. Bijeljic, "The impact of bimodal pore size distribution and wettability on relative permeability and capillary pressure in a microporous limestone with uncertainty quantification," *Advances in Water Resources,* vol. **171** (2023)

[13] S. Masalmeh, I. Abu Shiekah and X. Jing, "Improved Characterization and Modeling of Capillary Transition Zones in Carbonate Reservoirs," *SPE Reservoir Evaluation & Engineering,* SPE 109094-PA (2007)

[14] G. Coats, L.-Z. Xiao and M. Prammer, NMR Logging Principals and Applications, Halliburton Energy Services, Houston (1999)

[15] B. Kenyon, R. Kleinberg, C. Straley, G. Gubelin and C. Morriss, "Nuclear Magnetic Resonance Imaging - Technology for teh 21st Centry," (1995) [Online]. Available: https://www.slb.com/-/media/files/oilfield-review/08951933.ashx.

[16] B. Swanson, "A Simple Correlation Between Permeabilities and Mercury Capillary Pressures," SPE 8234 (1980)

[17] H. Hill, O. Shirley and G. Klein, "Bound Water in Shaley Sands - Its Relation to Qv and Other Formation Properties," *Log Analyst,* May-June (1979)

[18] S. Masalmeh and J. X-D, "Capillary Pressure Characteristics of Carbonate Reservoirs: Relationship between Drainage and Imbibition Curves," in *The International Symposium of the Society of Core Analysts*, Thondheim (2006)

[19] C. Land, "Calculation of Imbibition Relative Permeability for Two- and Three-Phase Flow From Rock Properties," *Trans. AIME,* SPE-1942-PA (1942)

[20] J. Killough, "Reservoir simulation with history-depedent saturation functions," *SPEJ,* vol. **324** (1976)

[21] S. Masalmeh and L. Wei, "Impact of Relative Permeability Hysteresis, IFT Depenent and Three Phase Models on the Performance of Gas Based EOR Process," in *Abu Dhabi International Petroleum Exhibition & Conference*, Abu Dhabi, UAE (2010)